

Development of an Automated ECT System for Complex Geometries using a Point Cloud Input

Sheila Shafira

Abstract

Eddy current testing (ECT) is a widely used Non-destructive testing (NDT) technique for detecting surface and sub-surface defects in conductive materials. Testing on components with complex geometries is still typically done manually as it requires an experienced technician to perform scans along the contour of a complex surface. This manual inspection tends to be time-consuming, labour-intensive, and prone to human errors. Automation in this field is highly desirable as more modern components with complex geometries are manufactured in order to meet the functional and aesthetic requirements of the products. An automated ECT system that can provide an accurate and reliable safety inspection in a time-effective manner will be able to overcome the limitations of a manually performed ECT. This project aims to develop an automated ECT system using point cloud data of the specimen under testing as an input, with an offline scan path generation that can adapt to unknown complex surfaces without the need for CAD files or complex calibrations. Validations and experiments were conducted on specimen blocks with sinusoidal wave patterns to investigate the system's capability. The point cloud data of the specimen is acquired by a depth camera, which later undergoes several pre-processing steps to prepare the point cloud for Poisson surface mesh reconstruction. The Poisson surface mesh reconstruction was able to generate an accurate representation of the specimen, with 0.5mm average deviation from the actual geometry. An adaptive sampling-based method was developed to generate a set of predefined points on the surface with a constant hypotenuse distance through the contour of the geometry. The scan path planning algorithm ensures that the ECT probe is always oriented perpendicular to the surface, regardless of the local surface curvature and orientation. The automated scan is then performed by a 3-axis motorized linear stages, which was verified to have perfect accuracy in positioning when following the set of predefined scan path.

SUPERVISED BY DR ROBERT HUGHES

DEPARTMENT OF MECHANICAL ENGINEERING

UNIVERSITY OF BRISTOL
2023

Declaration

This project report is submitted towards an application for a degree in Mechanical Engineering at the University of Bristol. The report is based upon independent work by the candidate. All contributions from others have been acknowledged and the supervisor is identified on the front page. The views expressed within the report are those of the author and not of the University of Bristol.

I hereby assert my right to be identified as the author of this report. I give permission to the University of Bristol Library to add this report to its stock and to make it available for consultation in the library, and for inter-library lending for use in another library. It may be copied in full or in part for any bona fide library or research worker on the understanding that users are made aware of their obligations under copyright legislation.

I hereby declare that the above statements are true.



© Copyright, Sheila Shafira, 2023

Certification of ownership of the copyright in a dissertation presented as part of and in accordance with the requirements for a degree in Mechanical Engineering at the University of Bristol.

This report is the property of the University of Bristol Library and may only be used with due regard to the author. Bibliographical references may be noted but no part may be copied for use or quotation in any published work without prior permission of the author. In addition, due acknowledgement for any use must be made.

Table of Contents

Table of Contents.....	3
1. Introduction	4
1.1 Background	4
1.2 Aims and Motivation	4
2. Theory	5
2.1 Eddy Current Testing.....	5
2.2 Manual and Automated ECT Scan	6
2.3 Point Cloud Data.....	7
3. Methods.....	7
3.1 Framework.....	7
3.2 Point Cloud Acquisition.....	8
3.3 Point Cloud Processing.....	10
3.4 Path Planning	14
3.5 Experimental Validation	15
4. Discussion.....	17
4.1 Results	17
4.2 Limitations & Future Work	18
5. Conclusions.....	18
6. Acknowledgements	19
7. References	19

1. Introduction

1.1 Background

Complex freeform surfaces are widely used on parts in various industries from aerospace, automotive, to medical implant manufacturing industries in order to meet the functional and aesthetic requirements of the products [1]. The shape and geometry of these modern components present a challenge for safety inspection. For instance, CFM56 engine fan blade that is used a lot of Boeing aircraft models shown in Figure 1. Safety assurance to verify the integrity of these components are commonly done by Non-destructive Testing (NDT). Various NDT techniques are used to evaluate materials, structure, component, or system without causing damage [2]. Therefore, NDT can be done repeatedly and maintains serviceability after testing. Furthermore, NDT provides reliable and accurate results for quality assurance, while also providing excellent cost efficiency for some scenarios compared to destructive testing. It is also relatively quick to perform, which lowers downtime for companies, therefore saving money.



Figure 1: CFM56 Engine Fan Blade [3].

Over the past few years, various techniques to handle complex unknown surfaces have been researched, such as Computer-aided Design (CAD) and Computer-aided Manufacturing (CAM) [4]. However, in the NDT field, most inspections for complex surfaces are still manually performed. This is because manual inspection is more flexible than automatic inspection as it allows operators to easily adapt to changing inspection needs. Often parts that are designed identical, will have significant deviations from the CAD when manufactured, resulting in a significant challenge for precision NDT measurement which must be flexible to accommodate this manufacturing issues [5]. Eddy Current Testing (ECT) is one of the most common NDT techniques used in the aerospace industry, to detect defects in critical components such as engine blades, landing gears and wing spars [6]. Due to the complex geometries of these components, manual ECT is often performed to inspect areas that are difficult to reach using automated systems. Manual inspection is performed by experienced technicians who typically have to position and move appropriate NDT devices over the contour of the specimen surface. Manual inspection relies on the technician's skills and results in a very slow inspection process for large samples. The automation of this area is highly desirable especially in handling complex shaped components. The fundamental aims of automation within inspection process are to minimise downtime and variability of results and errors due to human factors.

The use of motorized linear manipulators and gantry designs has, for several years, provided the most stable and reliable conditions in terms of positioning accuracy [7]. This usually consists of two or three linear axes (X, Y and Z), and usually rotary axes (rotary table, probe orientation) to control the position of the object relative to the NDT device, or vice versa. Most of these systems are equipped with stepper motors or programmers which give signal position in quasi real time, so that their performance in terms of accuracy, resolution and inspection rate complies with manufacturer requirements [7].

1.2 Aims and Motivation

The motivation behind this project is to overcome the limitations of manual ECT systems that are time-consuming, labour-intensive, and prone to human errors. This results in a growing need for an automated inspection system that can provide a more accurate and reliable result in a time-effective manner. This project aims to develop an automated ECT system with an offline scan path generation that can adapt to unknown complex surfaces without the need for CAD files of the component and any complex calibration. The system is intended for use by NDT departments such as UNDT Lab at the University of Bristol, as it is possible for use and further development of the system to do

inspections on small components. The algorithm should also not be limited to use with a specific motorized stages system, making it versatile to integrate with other systems. The major objectives of this project are:

1. Acquiring point cloud data using a depth camera.
2. Develop an algorithm to process the point cloud data to use an input for the automated ECT system.
3. Generating predefined points on the surface for the linear stages path.
4. Create a MATLAB script that could send commands to the linear stages to do inspections automatically.
5. Validation of the system.

2. Theory

2.1 Eddy Current Testing

Eddy Current Testing (ECT) is one of the conventional NDT techniques used to inspect conductive materials for surface and sub surface flaws. ECT is a practically instantaneous NDT technique, whereas other techniques, such as liquid penetrant testing or optical inspection, would require time consuming procedures that makes it less suitable for some applications, such as wires, bars, tubes, or profiles in production line [8]. ECT is based on the principle of electromagnetism, particularly the inductive properties of alternating current [9]. Electromagnetism is a phenomenon where electrons pass through a conductor causing a magnetic field to develop concentrically around the conductor and perpendicular to its axis. In ECT, a probe containing coil of wire is placed in closed proximity of the surface of the test specimen. There are various coil designs used for ECT probes, which are focused on either sensitivity or coverage area [10]. Despite the variety of designs, all coils can be characterised by their impedance parameter, Z_o , which is given by:

$$Z_o = \frac{V_o}{I_o} = R_o + jX_o = \sqrt{R_o^2 + X_o^2} \quad (1)$$

where R_o is resistance, and X_o is the reactance. An alternating current pass through the coil, generating a time-varying magnetic field that induces eddy current in the conductive material. ECT is based on Faraday's electromagnetic induction law. Faraday discovered that a time-varying magnetic induction flux density induces currents in a conductor [11]. Faraday's law is given by equation below:

$$\varepsilon = -\frac{d\Phi_b}{dt} \quad (2)$$

where ε is electromotive force, and $\frac{d\Phi_b}{dt}$ is the time rate of change of the magnetic flux density. Therefore when an alternating energized coil of impedance Z_o approaches an electrically conductive material, circular eddy currents are induced on the surface of the material. The eddy currents generate a magnetic field that opposes the primary field, as why the sign is negative in equation. This opposing magnetic field weakens the primary field, resulting in the new imaginary part of the coil impedance decreasing proportionally as eddy current intensity in the test piece increases [10]. This impedance variations can be used to determine the material's properties, such as thickness, conductivity, and variations in surface or sub-surface structure, therefore can determine if there is any defect present in the material.

2.2 Manual and Automated ECT Scan

For a complex geometry object, ECT is commonly done manually. Inspection is usually performed using a handheld probe that is moved along the surface topology of the material under testing. The probe contains a coil that generates an electromagnetic field and a second coil that detects eddy currents induced in the material. When a defect is present in the material, such as a crack or a void, the eddy currents are disrupted, resulting in a change of the electrical signal detected by a probe. These changes are read by the operator to determine if there is a defect present on the material. To ensure that the surface of material is thoroughly scanned, the operator thoroughly moves the probe in a systematic pattern, such as back-and-forth or in a circular motion, over the entire surface of the material. Some of the limitations that comes with ECT is the probe tilt and lift-off effect, this is visualized in Figure 2. Variation of probe tilt contributes significantly to noise. Probe should be kept perpendicular to the surface during the entire operation for consistent results. The change in probe tilts will change the area of the component affected by magnetic field, which affects coil impedance and changes which orientation of cracks are detected. Eliminating probe tilt is usually straightforward for a flat surface inspection. However, it is a challenge for complex surfaces inspection. Lift-off effect is another major contributor to noise in ECT. As coil impedance is proportional to the distance of the coil from the material's surface, variations of distance would affect the results. Lift-off distance varies for different types of ECT probes, as it depends on the size, shapes and operating frequencies which affect their sensitivity to defects and their ability to maintain a good contact with the specimen surface [12]. In [13], it was investigated the effect of lift-off variations on aluminium plate. It was found that an optimum lift-off value was achieved at 3mm and detected obvious signal response differences at lift-off value of 2mm, hence, a 1mm lift-off variation would significantly affect the reading.

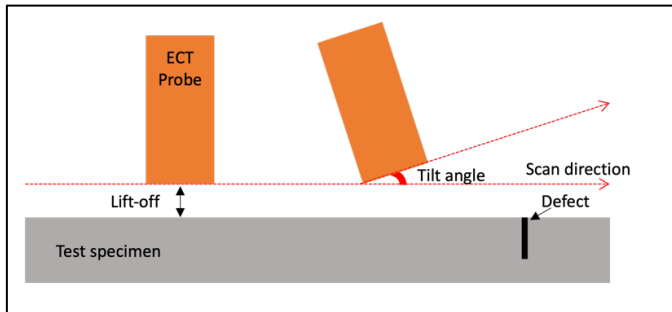


Figure 2: Diagram of ECT probe limiting factors.



Figure 3: Automated ECT system by Midas-NDT [15].

Manual ECT scanning requires trained technicians and results in a slow inspection process, especially for larger samples [14]. In addition, human error such as inconsistent probe tilt and lift-off could also be present thus affecting the results. Utilising a motorized system to perform ECT inspection provides a stable and reliable result as it may eliminates human error. Automated inspection using motorized stages provides accuracy by providing precise and repeatable movement of the object under test during scanning [14]. The automation of NDT has been a growing interest in engineering and a number of previous researchers have explored various methods in their work. Midas-NDT engineers have installed an automated ECT system at a UK service inspection company. Figure 3 shows the automated ECT system by Midas-NDT. Their automated ECT system generates an inspection pattern that allows inspection of a component without operator intervention. Inspection of the component's surface is performed by an eddy current probe mounted on a probe holder on an automated gantry system [16]. The system locates the gantry into its starting position, lower the probe onto the component's surface, and then commence a helical scan. The limitation to this system that it comes with a high cost, and the heavy machinery requires a difficult and long process of installation. Another similar example to this proposed system is a robotic NDT system using off-line scan path

planning in [17]. This work presents a computer-aided scan path generation for robotic NDT of complex -shaped specimens. This robotic NDT system utilises a six-axis robotic arm KUKA KR5 arc to perform an ECT scan on an aircraft wing with a positional uncertainty of the NDT scan less than 0.5mm [17]. Another work in NDT automation is presented in [2]. This work proposes a low-cost 1D geometry scanner for an intended use of ECT scanning for small complex geometries. The scanner was able to operate a geometry scanning with the perfect accuracy and precision measured to a resolution of 1mm [2].

2.3 Point Cloud Data

Point cloud is a set of discrete data points in space that usually represents a 3D shape of an object. It is commonly used in variety of application in the engineering industry, including path planning solution. A point cloud consists of a set of points with x, y, and z coordinates, and sometimes RGB colour values and even other attributes. Figure 4 shows an example of point cloud data expressing a 3D image. A common technique to store point cloud data in memory is to form an array, where each row of vector corresponds to a point [18].

Point cloud data can be captured in an accurate and efficient manner using various sensing technologies such as using a depth camera, 3D laser scanning and photogrammetry. Compared to other traditional measurement methods, such as manual measurement or electronic device-based measurement, point cloud data from sensing technologies have much higher measurement rate and better accuracy. A high-quality point cloud data would be a very accurate representation of an object, in other words, it would contain as many details of the object as possible. The advancement of cost-effective depth camera has made it possible to acquire point cloud data, which were previously only accessible using more expensive sensors such as time-of-flight cameras or 3D laser scanners. Structured light is one of the commonly used technologies in depth imaging. Structured light cameras project a pattern of light into the object, usually using infrared laser projector, and capture the deformation pattern as it is reflected by the object's surface [20]. The structured light patterns projected by the infrared laser projector create depth variations of the object's surface, which are captured by two sensors in the camera. These two sensors capture images of the object from slightly different angles, and the depth information is calculated by analysing the differences in the patters seen by each sensor. This process is repeated for multiple of frames to generate point cloud of the object. The point cloud data acquired by the depth camera needs to undergo pre-processing steps to create a surface mesh of the object, which can be used for variety of applications, including path planning.

3. Methods

3.1 Framework

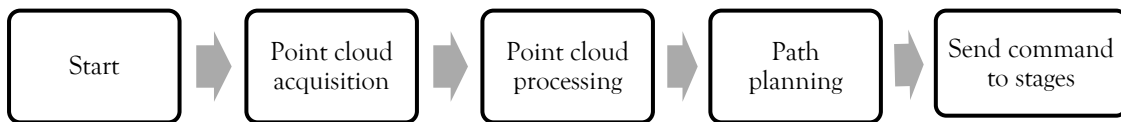


Figure 5: Flow diagram of the proposed system

The proposed system consists of a depth camera to acquire the point cloud data, 3-axis motorized linear stages to move the object relative to the eddy current probe, and a PC to control the stages. The system consists of 3 main

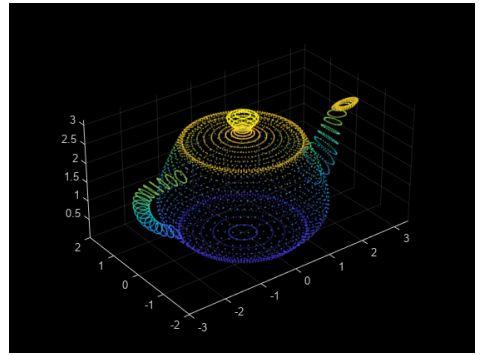


Figure 4: Example of a point cloud data [19].

steps, which are point cloud acquisition using the depth camera, point cloud processing and scan path planning on MATLAB. The output of these steps is a set of predefined points on the surface reconstruction of the specimen, which is then used to feed a command into the motorized stages to perform the automated eddy current inspection. Due to the time and cost constraints of this project, the system ability to adjust probe tilt was deemed out of the project scope and is discussed at the end of this report.

3.2 Point Cloud Acquisition

3.2.1 Depth Camera

The point cloud data used for this project was acquired using YDLIDAR OS30A 3D depth camera. The camera consists of two infrared (IR) cameras, a dot projector, and a depth processor. The dot projector is used to project a structured light pattern on the target scene, and the two IR cameras collect the structured light image of the target and depth calculation algorithm is executed to output the depth image of the target scene. The IR sensors in the two cameras allow images to be taken in low-light conditions. The depth processor calculates parallax according to the difference between the deviation values of the left and right camera pixels, then obtains the depth value. This camera adapts to complex environment, such as all-black environment, indoors with strong or weak light, and even semi-outdoor [21]. The camera has the specifications as shown below:

Table 1: Camera Specifications [19].

Resolution	1280x920 pixel
Horizontal Field-of-view (FOV)	78°
Vertical Field-of-view (FOV)	60°
Focal Length (Fx, Fy)	833mm
Principal Points (Cx, Cy)	Left Camera: 645.9mm (Cx) & 439.4mm (Cy) Right Camera: 658mm (Cx) & 463.1mm (Cy)
Detection range	200-2500mm

3.2.2 Set Up

Sets of point cloud data were acquired to conduct an experimental validation of the system. Aluminium blocks from a past student project were used as a test specimen for this experiment. These blocks are all 200x100x30mm in nominal directions, with variation of pattern with known sinusoidal function of z-direction along its x direction on its top surface as described in Table 2. These variations of sinusoidal functions were used to test this system's ability to follow the surfaces' topology.

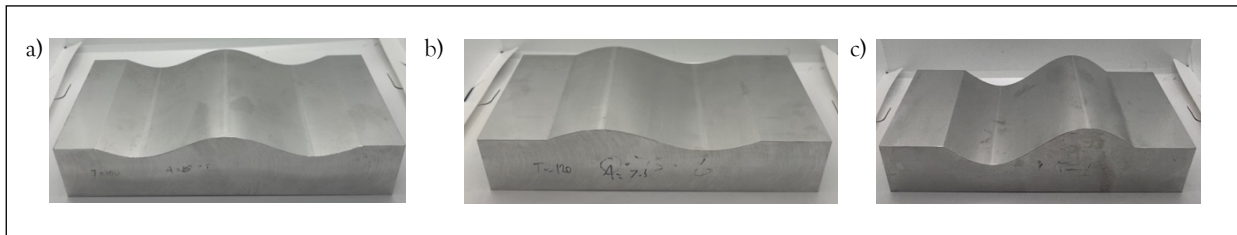


Figure 6: a) Block A. b) Block B. c) Block C

Table 2: Specimen Blocks Dimensions

Name	Length (mm)	Width, (mm)	Wavelength (mm)	Amplitude
Block A	100	200	150	7.5
Block B	100	200	150	7.5
Block C	100	200	140	15

Adjusting the distance between the camera and the object of interest affects the accuracy and resolution of depth data obtained from the camera. If the camera is too far away from the object, the IR light may become too diffused and the dot projected by the dot projector may become too sparse, on the contrary, putting the camera too close to the object may result in an over-saturated depth measurement. The distance between the camera and the object needs to be maintained between the camera's distance range. Angle of the camera relative to the object's region of interest also affects the coverage and the completeness of the 3D data obtained by the camera. However, when acquiring point cloud data, multiple images can be merged together using point cloud registration method where two or more point clouds in the same coordinate system are aligned into a single point cloud. This method ensures a complete and accurate generation of the object's point cloud representation.

The detection range of the camera was adjusted to 250-300mm, allowing it to only capture the region of interest, and ignoring objects outside the detection range. The object was placed approximately 22cm from the camera, and this enabled the camera to capture the object of interest completely. Multiple images were taken from multiple angles to be aligned using point cloud registration, discussed in the later section of the report. Figure 7 shows the set up for the image acquisition. The camera and the object were elevated for ease of post processing, therefore the image taken will need to be adjusted later and is discussed in Section 3.3.

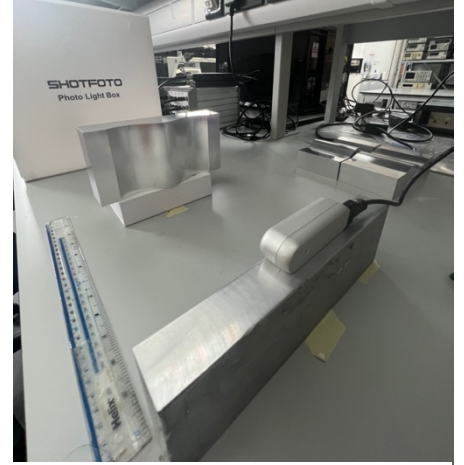


Figure 7: Set-up of the image acquisition

3.2.3 Depth Image to Point Cloud

Point cloud data was then produced using the depth information for each pixel, generated by the built-in depth processor, which uses the information of the two IR cameras with known parameters, such as their focal length and principal points. The process of generating point cloud data involves following steps:

1. Rectification: The captured images from the left and right IR cameras are first rectified to correct any distortion caused by the camera lenses. This step involves adjusting the images so that the principal points of the cameras are aligned and the Epipolar lines of the two cameras are in line to each other. Figure 8 shows the rectification process of two cameras placed horizontally. Epipolar plane is a plane in a 3D space containing the line of sight between the two cameras and the point being captured.

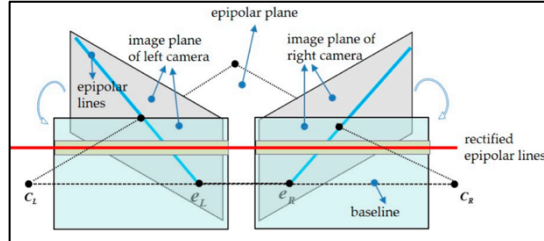


Figure 8: Diagram of rectification of two cameras. [22]

2. Disparity calculation: The depth processor uses the rectified images to calculate disparity, which is the difference in horizontal position of the same points in the two images. This is done by comparing the structured light pattern in each image which is used to determine the distance between the camera and the object.
3. Depth calculation: Using the disparity information and the camera's parameters, which is their focal length and the distance between two cameras, the depth processor calculates the distance between each point in the target scene and the camera that is the depth information of the image. Each depth value is represented by a pixel, corresponding between the camera and the object at that pixel. It is stored in a 2D coordinate system that defines the X and Y axes of the image, and each pixel in the image can be identified by its coordinates. The coordinates are typically stored in a matrix, where each pixel represents the distance of the image to the camera in millimetres.
4. 3D coordinate calculation: Finally, the depth information can be used to calculate the 3D coordinates of each point in the target scene. Using triangulation, the pixel coordinates and depth information are converted into 3D coordinates in a common reference frame which are combined into a point cloud, which represents 3D structure of the target scene. To compute the point cloud from a depth image, the depth pixel from the depth image 2D coordinate system is transformed to the depth camera 3D coordinate system. The 3D coordinates are computed using the following equations, where $depth(i, j)$ represents depth value at each row i and column j in the matrix:

$$z = depth(i, j) \quad (3)$$

$$x = \frac{(j - C_x) \times z}{F_x} \quad (4)$$

$$y = \frac{(i - C_y) \times z}{F_y} \quad (5)$$

Where x , y and z are the cartesian coordinates of each point in the point cloud, C_x and C_y are the principal points of the camera, and F_x , F_y are the focal points of the camera. The principal points and focal points of the camera intrinsic, obtained from calibrating the camera. YDLIDAR OS30A was factory calibrated, therefore the intrinsic was provided in the camera manual sheet. This depth camera has two IR cameras that are calibrated such that they have the same focal length value. The point cloud data is then stored in a .ply format, containing the location information of each point in x , y , and z coordinates.

3.3 Point Cloud Processing

The point cloud data acquired from the depth camera was further processed and analysed to create a 3D surface mesh of the object. Point cloud data produced by the depth camera contains noise, outliers, and so forth. These are also caused by random effects such as interference of the external environment, the stability of the camera during image acquisition, and the complexity of the surfaces. Therefore, pre-processing must be carried out before reconstructing the point cloud into a surface mesh. In general, processing steps such as registration, filtering, and smoothing are needed to generate a smooth and continuous surface for the scan path planning process.

3.3.1 Point Cloud Registration

To ensure a complete representation of the object, point cloud registration was performed to align multiple images. This is because acquiring a point cloud from a depth image are often incomplete, noisy and contain sources of

measurement error. Point cloud registration enables aligning multiple point clouds into a single and coherent 3D representation of the scene. An Iterative Closest Point (ICP) algorithm was used in this application, which works by iteratively minimizing distance between corresponding points in the two point clouds being registered [23].

3.3.2 Filtering

a) Adjusting the point cloud and removing outliers

Outliers are points which are away from the object and needs to be removed first. A manual outlier removal was done by adjusting the region of interest so that points that are not part of the object itself is removed from the point cloud space. This was done by cropping the point cloud so that only the boundaries of the object in interest are present in the point cloud space. The point cloud is then adjusted so that the object aligns with coordinate system axes. This was done by transforming the point cloud by translation and rotation until the point cloud aligns parallel with all 3 axes.

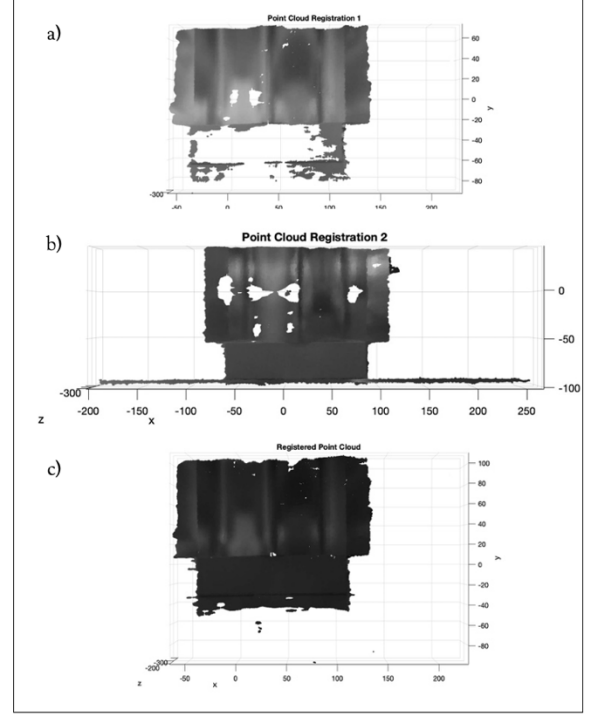


Figure 9: a) First point cloud. b) Second point cloud. c) Registered point cloud.

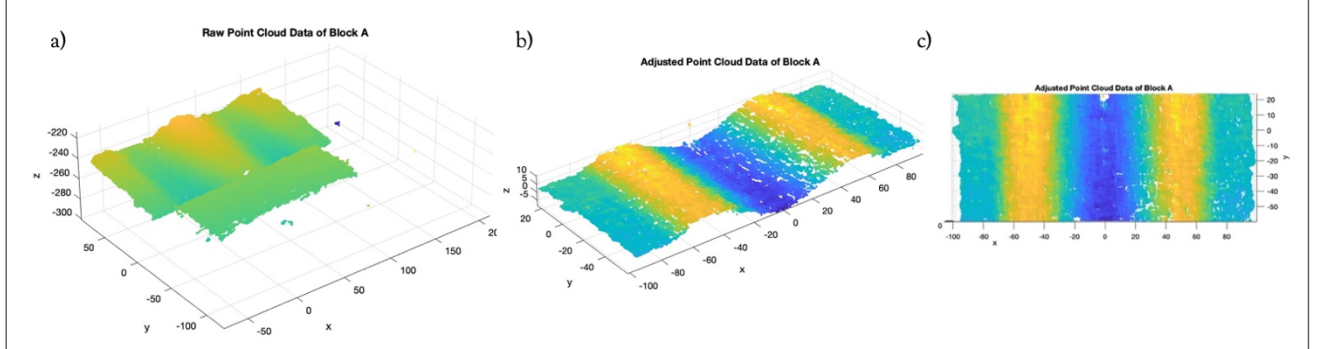


Figure 10: a) Raw point cloud data before processing. b), c) Point cloud data after adjusting, outliers removal and denoising.

b) Denoising

Noise is often produced when acquiring point cloud data using a scanning device. The filtering methods that are commonly used for denoising are gaussian filter and average filter. Gaussian filter is a filtering method used in image processing, where it uses a Gaussian smoothing operator to perform a weighted average surrounding pixel based on the Gaussian distribution [24]. The downside of this method is that it may blur or smooth out gradual changes on a surface, resulting in loss of details of the point cloud. Average filter was used for this application as it was relatively simple and efficient to apply to point cloud data. Sinusoidal surfaces tend to have a relatively low spatial frequency, meaning that the changes on the surface occurs gradually over a distance, making this filtering method a suitable method without sacrificing feature or edge detection and preservation. This filtering method works by replacing the value of each point with the average value of the neighbouring points. The result is a smoother surface on the point cloud where noise and random variations are reduced.

3.3.3 Surface mesh reconstruction

After adjusting the point cloud, removing outliers, and applying average filter to smooth out the surface of the point cloud, the point cloud was ready to be reconstructed into a surface mesh. Surface mesh reconstruction is necessary as there is an infinite number of surfaces that approximate a single point cloud, and a point cloud does not define a surface itself. Surface reconstruction from point clouds is a core topic in geometry processing of many applications, such as computer vision, robotics, and computer graphics [25]. There are different methods that can be used to effectively perform surface reconstruction such as Moving Least Squares, Delaunay Triangulation, and Poisson Surface Reconstruction. Moving Least Squares is a surface reconstruction method that uses local polynomial approximation to reconstruct a smooth surface from a set of point cloud data [26]. This method is particularly suitable to create a surface model with high accuracy and low approximation error, therefore it is widely used in applications where accuracy of the surface model. However, this method is computationally expensive because it involves solving local equations for each point in the point clouds. Another instance is Delaunay Triangulation, which is a method that works by reconstructing a mesh of non-overlapping triangles where each triangle circumference contains only a single point in the set of point clouds. This method is sensitive to noise and outliers in the point cloud data, making it less suitable for point cloud data input acquired from a depth camera which is generally noisy and contains outliers.

Poisson reconstruction method was used for this application as it performs well to approximate a noisy point cloud with a smooth surface [25]. On top of that, this method is generally more computationally efficient compared to the other methods. Poisson reconstruction method is an algorithm for reconstructing a surface mesh form an unorganized set of points with associated normals. The point cloud input used first needs to be processed to remove outliers and noise, this was explained in Section 3.3.2. Then, the algorithm consistently orients the surface normals. By solving the Poisson equation, it generates a field that determine the inside and outside of the object. The Poisson equation is shown in Equation (6), relating the Laplacian of an unknown function to its source density.

$$\nabla^2 f = \rho \quad (6)$$

where the input point cloud data is defined as a density function, ρ , and the surface reconstruction is defined as unknown function, f . After solving the Poisson equation, the generated data is organized into an octree data structure which allows efficient storage and processing. Octree data structure is a tree-based structure to represent a 3D space in a hierarchical manner that where items are divided into eight smaller octants [27]. An isosurface, representing the model's boundary is then extracted. The surface is then refined through some post processing techniques which results in a smooth surface representing the input point cloud data.

A built-in MATLAB function, *pc2surfacemesh* was used to generate the Poisson surface mesh [28]. This function takes the input of the point cloud data and a depth parameter. Depth parameter determines the octree used in the reconstruction algorithm. Octree is a tree data structure, which in this algorithm is used to partition the point cloud data into smaller regions, allowing for more accurate and efficient surface reconstruction. A higher depth value will result in a more detailed surface reconstruction, while lower value results in a smoother surface but loss in details. The Poisson reconstructed mesh contains faces, that approximate the input point cloud data, and vertices, which is the location where the edges of the mesh faces meet.

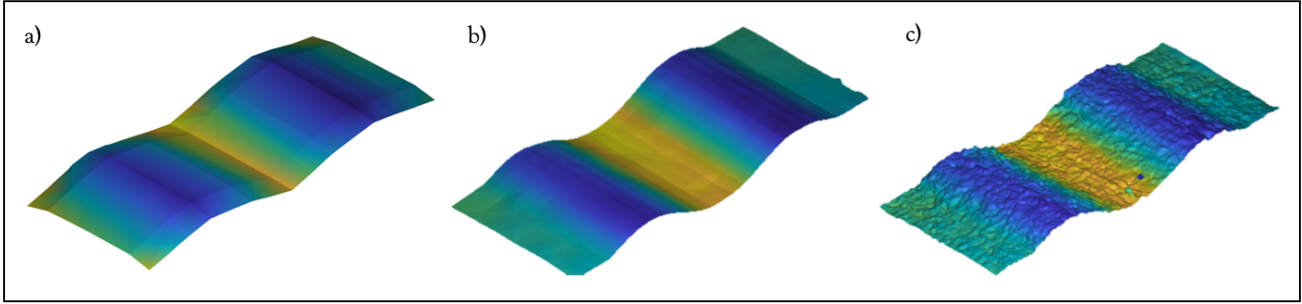


Figure 11: Poisson surface mesh reconstruction with depth value of: a) 3. b) 5. C) 7.

Figure 11 shows Poisson surface mesh reconstruction of block A with depth parameter values of 3, 5 and 7. A depth value of 5 was deemed suitable for this application, as it results in a visually smooth and continuous representation of the surface, yet still maintaining important details. To further evaluate the deviation of surface reconstruction for each depth parameter value, the variation in z axis were averaged and compared to a plot of the actual shape of the blocks to provide clarity as shown in Figure 12. Depth value of 5 was indicated to yield the least deviation from its actual shape compared to the other depth values.

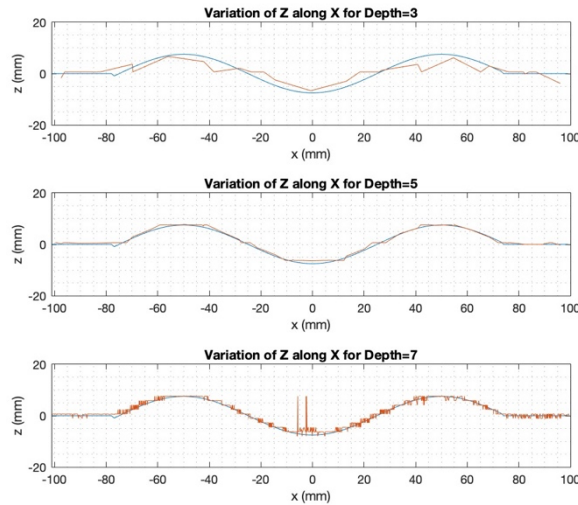


Figure 12: Plot of variation of Z along X for each depth parameter values.

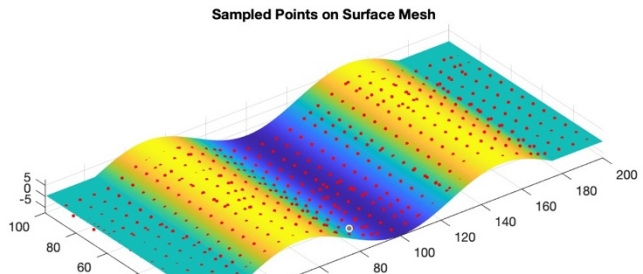


Figure 13: Sampled points of Poisson surface reconstruction on actual geometry.

The Poisson reconstructed mesh was then compared against its actual geometry to quantify the accuracy of the reconstruction. This was done by computing the point-to-space distance between points sampled on the surface mesh and the actual geometry using its known function. A uniformly spaced and dense set of points are generated on the Poisson reconstructed mesh to represent the location of the mesh vertices. To represent the actual geometry, a surface was generated by computing its known function. The sampled points were then overlaid on the actual geometry representation. By visual inspection as shown in Figure 13, the sampled points were able to represent the actual geometry without any significant differences. To validate the accuracy and reliability of the Poisson reconstructed mesh, the distance between the sampled points and the actual geometry are computed using point-to-space method. This was done by projecting the sampled points and finding the closest point on the surface mesh using its vertex. An average distance of 0.5mm was found between the points and the surface, resulting in 0.3% average error relative to the dimension of the actual geometry. This indicates that the error is relatively small and is considered insignificant for this application.

The root mean square error (RMSE) between the points and the surface was also calculated, to provide a measure of the average Euclidean distance between the Poisson reconstructed mesh and the actual surface geometry. This metric considers both the magnitude and direction of the differences between the reconstructed mesh and the actual geometry, therefore providing a measure of the overall geometric similarity of the surfaces. A RMSE value of 1.6mm was found, giving 0.7% error relative to the actual geometry dimension. The significance of these errors will be discussed in Section 4.1.

3.4 Path Planning

Once the surface mesh of the point cloud is created. The next step is to generate the scan path for the motorized stages to perform inspection. Scan path generation is a specific application of path planning, where the focus is on generating scanning paths for an optimized ECT scanning efficiency. This involves determining the path that the motorized stages will follow as they move the specimen under inspection relative to the ECT probe. Path planning process for this application involves selecting a set of points on the surface representation, defining the path between these points, and finally programming the motorized stages to move along this predefined path. The goal is to ensure that the probe covers the entire surface of the specimen by generating a sequence of points to be visited in a systematic manner. This ensures that the entire surface of the specimen is inspected with equal sensitivity and resolution.

There are several methods for scan path generation with different characteristics and suitability for various applications. Some of the most commonly used methods are grid-based methods and sampling-based method. Grid-based methods divide the specimen surface into a grid and generate a scan path by systematically traversing the grid in a predefined order. This is a relatively simple method but is not suitable to handle complex surface geometries [29]. This system proposes an adaptive sampling-based method to define set of points for the motorized stages path. The benefit of this method for this specific application are its flexibility, scalability, robustness, and computational efficiency. This method provides flexibility in path generation by sampling points and allows adaptability to the ECT scanning requirements. This method also provides scalability and robustness as it allows generation of sampled points based on the specific needs of the ECT scanning and the specimen size. Furthermore, it has a lower computational complexity compared to other methods that are usually more exhaustive.

A set of points are distributed across the surface with a variation of density based on the local surface feature. Compared to conventional scanning method such as raster scanning or encirclement scanning in common ECT application, this method offers several advantages. Raster scanning us commonly used in ECT on flat plates. This is done by moving the ECT probe in a series of parallel lines or rows over a specimen surface, resembling a grid pattern across the surface. The result of this scanning method is a large amount of data, even in regions where there are no significant variations of surface feature. Contrarily, adaptive sampling method allows adjustment in the sampling density for regions with greater variability, therefore minimizing the amount of data generated and improving efficiency of inspection process. In encirclement scanning, ECT probe is moved in a circular pattern around the specimen surface. This scanning method is commonly used for specimens with a circular geometry, such as pipes. However, this scanning method may not be suitable for non-circular geometries or surfaces with significant surface variability, bas the probe may not capture all region of the surface with equal sensitivity and resolution. Conversely, by using adaptive sampling method, scanning path can be adjusted to the surface characteristic of the specimen, ensuring adequate sample of all the surface regions.

The path planning for this application is constrained by probe tilt and probe lift off. The proposed sampling method algorithm ensures that the ECT probe remains in contact with the surface at all times during inspection and maintains constant probe lift-off distance throughout the whole scanning process. The motorized stages move the specimen under inspection on x, y, and z direction simultaneously by following a predefined path. The result is the

specimen moving relative to ECT probe mounted on top of the stages. The relative orientation of the ECT probe, however, will need to adapt to the specimen surface to remain normal orientation, but this is beyond the scope of this research project and will be discussed in Section 4.2.

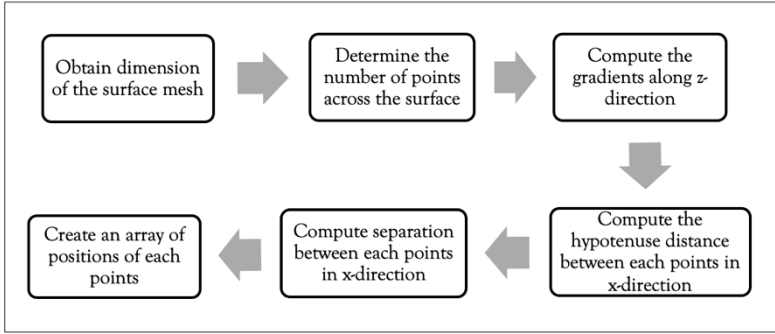


Figure 14: Flow diagram of adaptive sampling method

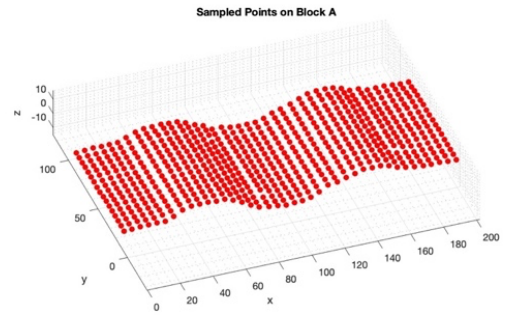


Figure 15: Sampled points on Block A

The proposed algorithm shown in Figure 14 works by keeping a constant hypotenuse distance through the contour of the geometry, this ensures that the ECT probe is always oriented perpendicular to the surface, regardless of the local surface curvature and orientation.

The number of points sampled across the surface depends on the spatial coverage of the ECT probe used for the inspection. For example, for a small ECT probe with a 5 mm spatial coverage, then the sampled points on a 200 mm length specimen would be 40 points, this is shown in Figure 15. The algorithm then computes the separations between each point in x-direction to achieve 5 mm separation between these points, by taking the gradients along the z-direction and computing the hypotenuse distance between each point in x-direction. This algorithm allows the system to adapt to any surface topology, without the need of any manual input from the operator regarding the surface feature.

3.5 Experimental Validation

3.5.1. Experiment Set Up

To quantify the operation of this automated ECT system, experiments were conducted to determine the accuracy of the motorized stages positioning against the set of predefined points. The motorized linear stages used for the experiment is the Zaber stages in the UNDT Lab of the University of Bristol. It is a compact-sized computer-controlled 3-axis motorized stages with built-in manual controller. The device is excellent for applications when small profiles are required and allows stage positions to be recalled accurately after each movement [30]. The device is set fixed on a platform to restrict unwanted movement. An ECT probe is mounted on top of the stages, and it can be replaceable with different types of probes, this is shown in Figure 17.

Three motorized linear stages are chained into a 3-axis stages as shown in Figure 16, consisting of: X-LSM200A moving in the x-direction, X-LSM200A moving in the y-direction and X-VSR40A moving in the z-direction. The specifications of the motorized stages are shown below in Table 3:

Table 3: Specifications of motorized stages

Series	Travel Distance	Accuracy	Axis
X-LSM200A	203.2mm	60µm	X and Y
X-VSR40A	40mm	35µm	Z

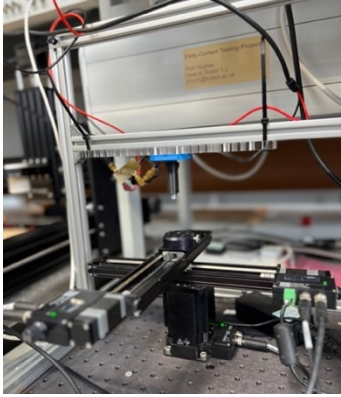


Figure 16: Motorized stages set up.

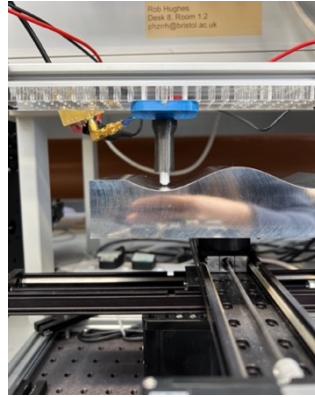


Figure 17: Probe normal to the specimen.

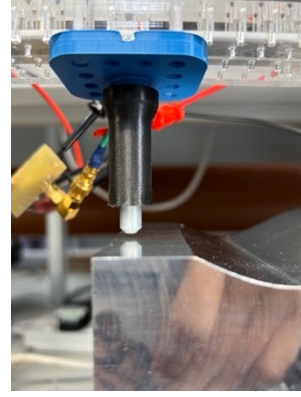


Figure 18: Home position

The motorized stages were controlled using MATLAB. However, this motorized system supports various programming software such as Python, Java, and C++. Using USB serial communication, the stages were able to receive and execute commands from MATLAB.

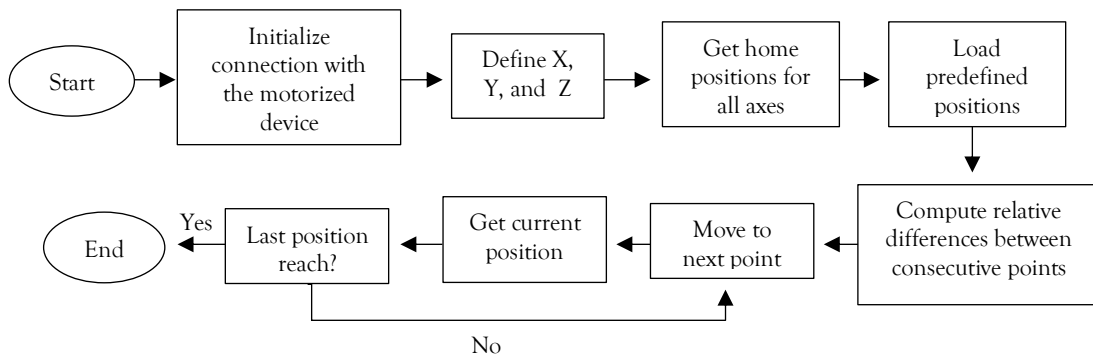


Figure 19: Flow diagram of the motorized stages command script

The flow diagram of the motorized stages MATLAB script is shown in Figure 19 above. Once the motorized stages connection with MATLAB is initialized, each device is assigned an axis. Using the manual controller, the stages were moved to a home position. For this experiment, the stages were moved into the far-left position of the specimen as shown in Figure 18, and the current position is set as home.

To measure the accuracy of the motorized stages to the given points, experiments were performed to obtain the accuracy of the motorized stages in following the predefined path. Then, the motorized stages were able to record the positions of each axis of the stages after each point are visited. In the first experiment, the motorized stages were given the instruction to follow the predefined points of block A in x and z direction. In the second experiment, the motorized stages were given the instruction to follow the same predefined points but with variations in the y direction. Experiments were also performed on the other specimen blocks to identify any anomalies in the results.

3.5.2. Experiment Result

The predefined points were generated using the adaptive sampling method on block A, with dimensions shown in Table 2 on Section 3.2.2.

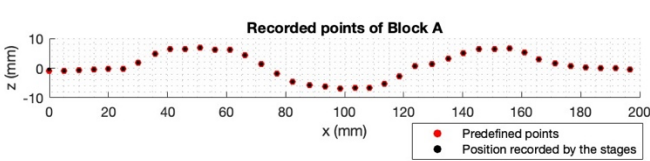


Figure 20: Predefined points of block A and the positions recorded by the stages.

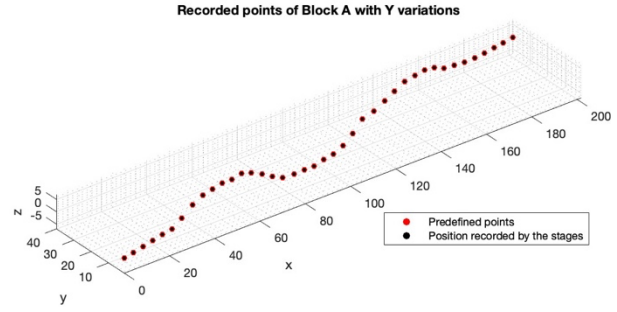


Figure 21: Predefined points of block A with Y variations and the positions recorded by the stages.

The results for the experiment of the x and z axis are shown in Figure 20. The positions recorded by the stages after each visited point are compared against the set of predefined points. It was found that the results of the x axis have the mean error as small as $0.002\mu\text{m}$ and a standard deviation of $0.012\mu\text{m}$. For the z axis, a mean error of $11.73\mu\text{m}$ and a standard of $74.11\mu\text{m}$ were obtained.

Figure 21 shows the results for the second experiment, where variations in the y axis are added. The results were the same for the x and z axis, with a mean error of $0.002\mu\text{m}$ and a standard deviation $0.013\mu\text{m}$ obtained for the y axis. To identify any anomalies in the experiment results, the same experiments were also performed using predefined points generated by the adaptive sampling method on block B and block C, where the same results were also obtained.

These results conclude that the motorized stages have perfect accuracy in following the predefined points. The result for the z axis is critical to determine the suitability of the motorized stages to maintain a constant lift-off distance. As discussed in Section 2.2, a lift-off variation of 1 mm would significantly affect the reading. Hence, the z-axis motorized linear stage used in this experiment is suitable for this system as it resulted in very small lift off variation much smaller than 1mm.

4. Discussion

4.1 Results

The point cloud data acquired by the depth camera was able to generate a point cloud representation of the object in interest, which was effectively reconstructed into a surface mesh using Poisson reconstruction method. Before the surface reconstruction process, the raw point cloud data had to undergo several processing steps in order to fill the missing information using the registration process, removing outliers captured in the depth images, and reduce noise so that a smooth surface mesh can be generated. These serials of processes were programmed in MATLAB. However, the processing steps were relatively simple, and the algorithm should be able to adapt to other complex geometries. By only a set of .ply files of a specimen as an input, the developed algorithm should be able to process the complex unknown geometry and prepare it for the scan path planning process. The algorithm developed for scan path generation is capable to generate adaptive sample-based points using the Poisson surface reconstruction as an input. This algorithm will not need any manual input from the user, as it should automatically produce points by taking information from the Poisson surface reconstruction.

The proposed automated ECT system was validated at different stages. The capability of the system was first investigated by evaluating the surface reconstruction accuracy against its actual geometry. The Poisson reconstruction method was able to create a surface reconstruction of the point cloud acquired with a good accuracy. The average deviation of the surface reconstruction and the actual geometry was obtained to be 0.5mm, with 0.3% error relative to the dimension of the geometry, and an RMSE of 1.6mm, giving 0.7% error relative to the actual geometry dimension. This error is considered very small and insignificant for this application. However, this error may be significant for more complex geometries that require higher accuracy. Therefore, future work can be done in developing a more robust algorithm for surface reconstruction that allows a more accurate reconstruction.

The motorized stages were capable in following the predefined path with perfect accuracy. The motorized stages were also able to maintain constant probe lift-off distance, which is commonly a source of error in a manual inspection. The use of motorized stages also significantly reduces the inspection time and complexity of the scanning process as the only step that needs to be taken is running the MATLAB script, and the motorized stages would follow the specimen surface in a systematic and comprehensive manner according to the commands. The system is also able to reduce the complexity of a manual ECT scanning which requires operator to carefully maintain ECT probe positions and lift-off distance, as the motorized stages automatically scan the specimen surface and follows its geometry by following the MATLAB command. A consistent scanning speed is also maintained throughout the inspection process, unlike manual inspection that often takes longer time due to factors such as fatigue and inconsistency. Another benefit to this system is that it can operate continuously for extended period. This results in increased productivity and reduced inspection time.

4.2 Limitations & Future Work

There are some limitations to this system due to the devices used in the experiments. For the point cloud input, the data acquired by the YDLIDAR OS30A Depth Camera contained noise and holes. The common reason for holes in point clouds acquired by a depth camera is occlusions. Occlusions are areas where information are not captured. This occurs due to the relative placement of the dot projector and the IR camera, creating blind spots on the target scene. This problem would be significant if the specimen under inspection is far more complex than the specimens used in this research project. To overcome this problem, time-of-flight cameras could be used to acquire point cloud data as it is capable to capture this missing information that are not able to be captured by a depth camera.

Another limitation comes from the motorized stages used in this project. The motorized stages used for the experiments had limited travel distance on all axes, therefore, only small specimens can be inspected using this device. Inspection for larger specimen would need a motorized stages with bigger range of motion. Various type of motorized stages is available on the market with variation of sizes and travel distance. The algorithm should be capable for use with different motorized stages with slight adjusting to the MATLAB script.

For further development of this system, integrating a tilt stage for the ECT probe would overcome the limitation of the probe orientation. Integration of a tilt stage system would allow the ECT probe orientation to change relative to the specimen and keeping normal to the surface. Another potential development area is the optimization of path planning for the automated scanning. Further research on path planning algorithms can be done to determine the most efficient path for inspection from the starting point to the end point.

5. Conclusions

In conclusion, the proposed system is deemed appropriate to an extent use of automated ECT scanning. It was able to follow complex geometries using only a point cloud input from the depth camera. Validation and experiments were carried out to investigate the capability of the system. Point cloud data was produced from depth images acquired by the depth camera. The point cloud data was further processed and analysed to create a 3D surface mesh representation of the complex geometry. The surface reconstruction was generated using Poisson reconstruction method and the accuracy of the reconstruction compared to the actual geometry were investigated. Then, the surface reconstruction was used to produce a scanning path, where an adaptive sampling-based method were used to generate a set of points with constant hypotenuse distance through the contour of the geometry to ensure that ECT probe maintains perpendicular orientation to the specimen surface. Experiments were carried out with the motorized stages to determine its accuracy in following the predefined path. The motorized stages were able to carry out the scanning process with excellent positioning accuracy in x, y, and z directions. The excellent positioning accuracy in z-direction ensures a constant probe lift-off distance, which satisfies ECT scanning requirement. This system has benefits over manual ECT, by providing a time and labour efficient inspection system with reliable and accurate results. Lastly, limitations of this system were discussed to evaluate potential developments to achieve an automated ECT system that is capable in performing a fully automatic inspection on complex geometries.

6. Acknowledgements

The author wishes to acknowledge Dr. Robert Hughes and thank him for providing guidance and supervision throughout this whole research project, and Alexis Hernandez from the UNDT Lab for providing guidance on how to operate the Zaber stages.

7. References

1. M. Dhanda and S. Pande, "Adaptive Tool Path Planning Strategy for Freeform Surface Machining using Point Cloud," *Computer-Aided Design and Applications*, vol. 16, no. 2, pp. 289–307, Aug. 2018, doi: <https://doi.org/10.14733/cadaps.2019.289-307>.
2. J. Milsom, "Design and Control of a Low Cost 1D Complex Geometry Scanner for NDT", *University of Bristol*. 2021.
3. "Available Repair Scope Basic Overhaul: Engine Manual Section 72-21-01." <https://www.gknaerospace.com/globalassets/downloads/aerospace-fan-blade-repair-capabilities/cfm-56-7b-fan-blade.pdf/>.
4. F. Nagata *et al.*, "Generation of normalized tool vector from 3-axis CL data and its application to a mold polishing robot," *IEEE Xplore*, Sep. 01, 2004. <https://ieeexplore.ieee.org/document/1390035>.
5. C. Mineo, S. G. Pierce, P. I. Nicholson, and I. Cooper, "Robotic path planning for non-destructive testing – A custom MATLAB toolbox approach," *Robotics and Computer-Integrated Manufacturing*, vol. 37, pp. 1–12, Feb. 2016, doi: <https://doi.org/10.1016/j.rcim.2015.05.003>.
6. "Aircraft testing," *Okondt.com*, 2021. <https://www.okondt.com/applications/aircraft-testing/eddy-current-testing-of-aircraft>
7. P. Louvion, A. Tachattahte, and D. Garnier, "Robotised UT Transmission NDT of Composite Complex Shaped Parts." Available: <https://www.ndt.net/article/aero2012/papers/we3b2.pdf>
8. Mercier, D. *et al.*, "Eddy currents and hardness testing for evaluation of steel decarburizing" *NDT E, Int.* 2006, 39, 652-660.
9. R. Bogue, "The role of robotics in non-destructive testing," *Industrial Robot: the international journal of robotics research and application*, vol. ahead-of-print, no. ahead-of-print, Sep. 2019, doi: <https://doi.org/10.1108/01439911011063236>.
10. G. Karanikos , "Low-drag, Low-friction Eddy Current Testing Rig for Complex Geometries", *University of Bristol*, 2020.
11. J. García-Martín, J. Gómez-Gil, and E. Vázquez-Sánchez, "Non-Destructive Techniques Based on Eddy Current Testing," *Sensors*, vol. 11, no. 3, pp. 2525–2565, Feb. 2011, doi: <https://doi.org/10.3390/s110302525>.
12. Paul E. Mix, *et al.*, "Introduction to Nondestructive Testing: A Training Guide, 2nd Edition", *John Wiley & Sons*. 2012, 95-96.
13. S. Salmia, F. Sulaiman, and E. Folly Eldy, "Optimisation Frequency for Different Lift off on Aluminium using Eddy Current Testing (ECT) Technique," *Transactions on Science and Technology*, vol. 6, no. 2–2, 2019, Accessed: May 13, 2023. [Online]. Available: <https://tost.unise.org/pdfs/vol6/no2-2/6x2-2x191-197.pdf>
14. C. Mineo, S. G. Pierce, P. I. Nicholson, and I. Cooper, "Robotic path planning for non-destructive testing – A custom MATLAB toolbox approach," *Robotics and Computer-Integrated Manufacturing*, vol. 37, pp. 1–12, Feb. 2016, doi: <https://doi.org/10.1016/j.rcim.2015.05.003>.

15. V. Patankar, V. Joshi, and B. K. Lande, "Development of an Automated - Ultrasonic Gauging System for Tubes and Pipes," www.semanticscholar.org, 2006. <https://www.semanticscholar.org/paper/Development-of-an-Automated-Ultrasonic-Gauging-for-Patankar-Joshi/ed3d6cee923e4bb9fc48d0654dd9ac98b63eb878>.
16. "Midas installs automated eddy current inspection system," www.bindt.org. <https://www.bindt.org/News/may-2010/Midas-installs-automated-eddy-current-inspection-system/?cookie-accept=1>.
17. M. Morozov, S. G. Pierce, C. N. MacLeod, C. Mineo, and R. Summan, "Off-line scan path planning for robotic NDT," *Measurement*, vol. 122, pp. 284-290, Jul. 2018, doi: <https://doi.org/10.1016/j.measurement.2018.02.020>.
18. A. Kadambi, A. Bhandari, and R. Raskar, "3D Depth Cameras in Vision: Benefits and Limitations of the Hardware," *Computer Vision and Machine Learning with RGB-D Sensors*, pp. 3-26, 2014, doi: https://doi.org/10.1007/978-3-319-08651-4_1.
19. "Read 3-D point cloud from PLY or PCD file - MATLAB pcread - MathWorks United Kingdom," uk.mathworks.com. <https://uk.mathworks.com/help/vision/ref/pcread.html>.
20. "Optica Publishing Group," opg.optica.org. <https://opg.optica.org/aop/fulltext.cfm?uri=aop-3-2-128&id=211561>.
21. "YDLIDAR|Focus on lidar sensor solutions," www.ydlidar.com. [https://www.ydlidar.com/Public/upload/files/2022-11-30/BMVM OS30A%20Data%20Sheet%20V1.0%20\(221130\).pdf](https://www.ydlidar.com/Public/upload/files/2022-11-30/BMVM OS30A%20Data%20Sheet%20V1.0%20(221130).pdf)
22. F. Gu, Z. Song, and Z. Zhao, "Single-Shot Structured Light Sensor for 3D Dense and Dynamic Reconstruction," *Sensors*, vol. 20, no. 4, p. 1094, Feb. 2020, doi: <https://doi.org/10.3390/s20041094>.
23. Z. Zhang. "Iterative point matching for registration of free-form curves and surfaces". *International Journal of Computer Vision*. 13 (12): 119–152. <https://citeseerx.ist.psu.edu/viewdoc/summary?doi=10.1.1.175.770>
24. "Gaussian Filtering - Computer Vision Website Header," www.southampton.ac.uk. https://www.southampton.ac.uk/~msn/book/new_demo/gaussian/#:~:text=The%20Gaussian%20Smoothi ng%20Operator%20performs
25. "CGAL 5.5.2 - Manual: Surface Reconstruction from Point Clouds," doc.cgal.org. https://doc.cgal.org/latest/Manual/tuto_reconstruction.html.
26. J. H. Cadwell, "A Least Squares Surface Fitting Program," *The Computer Journal*, vol. 3, no. 4, pp. 266–269, Apr. 1961, doi: <https://doi.org/10.1093/comjnl/3.4.266>.
27. "Octree - an overview | ScienceDirect Topics," www.sciencedirect.com. <https://www.sciencedirect.com/topics/mathematics/octree>.
28. "Construct surface mesh from 3-D point cloud - MATLAB pc2surfacedmesh - MathWorks United Kingdom," uk.mathworks.com. <https://uk.mathworks.com/help/lidar/ref/pc2surfacedmesh.html>.
29. K. Ryu, L. Dantanarayana, T. Furukawa, and G. Dissanayake, "Grid-based scan-to-map matching for accurate 2D map building," *Advanced Robotics*, vol. 30, no. 7, pp. 431–448, Mar. 2016, doi: <https://doi.org/10.1080/01691864.2015.1124025>.
30. "Zaber Technologies," www.zaber.com. <https://www.zaber.com/products/linear-stages>.